# The Potential of DAS in Teleseismic Studies: Insights From the Goldstone Experiment

Chunquan Yu[1,2], Zhongwen Zhan[1], Nathaniel J. Lindsey[3,4], Jonathan B. Ajo-Franklin[4], and Michelle Robertson[4]

[1] Seismological Laboratory, California Institute of Technology, Pasadena, CA, USA, [2] Now at Department of Earth and Space Sciences, Southern University of Science and Technology, Shenzhen, China, [3] Earth and Planetary Science Department, University of California, Berkeley, CA, USA, [4] Energy Geosciences Division, Lawrence Berkeley National Laboratory, Berkeley, CA, USA

Correspondence to: C. Yu, yucq@sustc.edu.cn

## Abstract

Distributed acoustic sensing (DAS) is a recently developed technique that has demonstrated its utility in the oil and gas industry. Here we demonstrate the potential of DAS in teleseismic studies using the Goldstone OpticaL Fiber Seismic experiment in Goldstone, California. By analyzing teleseismic waveforms from the 10 January 2018 M7.5 Honduras earthquake recorded on ~5,000 DAS channels and the nearby broadband station GSC, we first compute receiver functions for DAS channels using the vertical-component GSC velocity as an approximation for the incident source wavelet. The Moho *P*-to-*s* conversions are clearly visible on DAS receiver functions. We then derive meter-scale arrival time measurements along the entire 20-km-long array. We are also able to measure path-averaged Rayleigh wave group velocity and local Rayleigh wave phase velocity. The latter, however, has large uncertainties. Our study suggests that DAS will likely play an important role in many fields of passive seismology in the near future.

## Plain Language Summary

Distributed acoustic sensing (DAS) is a newly developed technique that transforms telecommunication fiber optic cables into linear arrays of ground-motion sensors. It has received much attention in the oil and gas industry recently. In this study, we conduct the Goldstone OpticaL Fiber Seismic experiment in Goldstone, California, and explore the potential of DAS in passive seismology using distant earthquakes. We first show that seismic data from the 10 January 2018 M7.5 Honduras earthquake recorded by DAS are of high fidelity by comparing them with that on a nearby broadband seismometer. We then demonstrate the utility of DAS in passive earthquake seismology, including receiver function analysis, densely distributed travel time measurements, and Rayleigh wave group/phase velocity estimation. These applications can potentially be used to provide high-resolution structural images of the crust and mantle. Thus, DAS will likely play an important role in many fields of passive seismology in the near future.

## 1 Introduction

Distributed acoustic sensing (DAS) is a newly developed technique that transforms telecommunication fiber optic cables into linear arrays of ground-

motion sensors (Grattan & Meggitt, 2000; Posey et al., 2000). Two major advantages of DAS, compared with conventional ground-motion sensors, come from its dense spatial sampling and cost-effective installation (Lumens, 2014). Recently, DAS has received much attention in the oil and gas industry and has shown its utility in reservoir surveillance (e.g., Daley et al., 2013; Lumens, 2014; Mateeva et al., 2014) and vertical seismic profiling (e.g., Bakku, 2015; Mateeva et al., 2012; Miller et al., 2012).

The application of DAS in passive earthquake seismology, however, is still at its early stage. Several field experiments have been carried out recently. For example, Lindsey et al. (2017) analyzed regional/teleseismic earthquake waveforms from three different DAS arrays in Alaska and California. They found that DAS waveforms show a high degree of correlation with a colocated seismometer record. In the PoroTomo experiment in Nevada, Wang et al. (2018) also found coherent earthquake waveforms recorded at a dense DAS array and a dense geophone array from a local $M_L$ 4.3 event. Li and Zhan (2018) applied template matching to the PoroTomo DAS data and detected over 100 earthquakes based on five cataloged earthquakes. Jousset et al. (2018) demonstrated the possibility of using DAS data for subsurface fault zone imaging. Zeng et al. (2017) extracted noise cross-correlation functions from a DAS array at Garner Valley, California. Dou et al. (2017) used traffic noise interferometry for seismic monitoring of the near-surface structure.

The great consistency of earthquake waveforms recorded by DAS and by conventional seismometers (e.g., Ajo-Franklin et al., 2019; Lindsey et al., 2017; Wang et al., 2018), the observations of broadband sensitivity on DAS (Ajo-Franklin et al., 2019; Becker et al., 2017), and the availability of existing telecommunication infrastructures (e.g., Ajo-Franklin et al., 2019; Jousset et al., 2018; Lindsey et al., 2017) motivate us to provide more in-depth analyses of DAS earthquake waveforms. Here we explore the potential applications of DAS to teleseismic studies using the Goldstone OpticaL Fiber Seismic (GOLFS) experiment in Goldstone, California. Using waveforms from the 10 January 2018 M7.5 Honduras event, we first show that dynamic strains recorded by DAS are of high fidelity by comparing them with horizontal velocities on the nearby broadband seismometer GSC. We then demonstrate the utility of DAS in teleseismic studies, including receiver function analysis, densely distributed travel time measurements, and Rayleigh wave group/phase velocity estimation. These applications can potentially be used to provide high-resolution structural images of the crust and mantle.

## 2 Data and Methods

### 2.1 Fiber Optic Cable as a Dense Array of Strainmeters

DAS relies on Rayleigh scattering from ubiquitous internal scatters throughout a fiber optic cable (Posey et al., 2000). These scatters are due to natural inhomogeneities caused by the fiber manufacturing process. During

the DAS measurement, coherent laser pulses are sent out from the interrogator unit to the fiber cable at constant time intervals. Reflected energy is continuously scattered back to the interrogator unit. The changes of phase difference between two ending points of each segment, which is caused by axial dilations or compressions, are used to measure strains (or strain rates) at distributed segments along the fiber optic cable (e.g., Hartog et al., 2014; Lumens, 2014). The typical gauge length of DAS is about 8–10 m, sampled at spatial windows as small as 0.25 m. To this end, DAS effectively transforms a fiber optic cable into a dense array of strainmeters. Currently, the maximum DAS sensing range is between 10 and 35 of kilometers depending on fiber type and interrogator characteristics.

The relationship between strain (spatial derivative of displacement) and particle velocity (temporary derivative of displacement) has been widely documented in the literature (e.g., Agnew, 1986; Benioff, 1935; Daley et al., 2016; Gomberg & Agnew, 1996; Langston & Liang, 2008; Mikumo & Aki, 1964). For plane wave incidence, strain is related to particle velocity through the following equation

$$\varepsilon_{xx} = -\frac{1}{c}\dot{u}_x, \quad (1)$$

where $\varepsilon_{xx}$, $\dot{u}_x$, and $c$ are strain, particle velocity, and apparent phase velocity along the cable axial direction $\vec{x}$ (distance from the interrogation unit increases), respectively. In the case of teleseismic wave incidence, plane wave approximation is generally valid. The apparent phase velocity varies for different seismic phases and is positive if the angle between the cable axial direction $\vec{x}$ and the wave propagation direction is less than 90°. In the supporting information, we further demonstrate the angle dependence of $\varepsilon_{xx}$ for *P*, *SV*, and *SH* particle motions (e.g., Benioff, 1935; Lindsey et al., 2017; Martin et al., 2018).

Equation 1 provides the basis for several potential applications of DAS in teleseismic studies. First, waveforms of DAS strains should look similar to particle velocities in the same axial direction except for a 0° or 180° phase shift and an amplitude modulation by the apparent phase velocity (between 0 and the inverse of phase velocity). Thus, DAS can be used to derive densely distributed phase arrival time measurements. Second, in the *P* wave train, DAS strain waveforms are always in phase regardless of the cable orientation and have a polarity flip with respect to the radial-component particle velocity (supporting information). If an approximation of incident source wavelet can be generated, DAS channels can then be used for conventional receiver function analysis. Third, equation 1 can potentially be used to determine local phase velocity by intercomparison of waveform amplitudes from colocated strainmeter and seismometer (Gomberg & Agnew, 1996; Mikumo & Aki, 1964).

## 2.2 The GOLFS Experiment

The GOLFS experiment was carried out between 2017 and 2018 in Goldstone, California. The experiment utilized an existing telecommunication fiber optic cable around the Goldstone Deep Space Communications Complex, which forms a horizontal loop geometry with a totally length of ~50 km (Figure 1). The original cable was installed in a double walled conduit, the majority of which is buried underneath the surface. In November 2017 to February 2018, a DAS interrogator unit (Silixa iDAS v2) was installed at the Apollo site to record dynamic strain rate measurements along a ~20-km-long segment (Figure 1). The gauge length of the system is set at 10 m, and the channel spacing is 4 m. There are ~5,000 channels in total, and data were integrated to strain. Conventionally, tap tests using multiple hammer shots have been used to map physical locations to DAS channel numbers. However, due to limited access to the cable route in the now protected wilderness area to conduct enough tap tests, we take a different approach here. We use recorded teleseismic waveforms to first locate some key channel numbers where there are sudden changes of cable orientations (Figure 1) and then interpolate between them. We note that for higher frequency studies and finer-scale problems, tap tests are still necessary. In this study, we also use broadband waveform data from the GSC station, which is located near the GOLFS experiment (Figure 1).

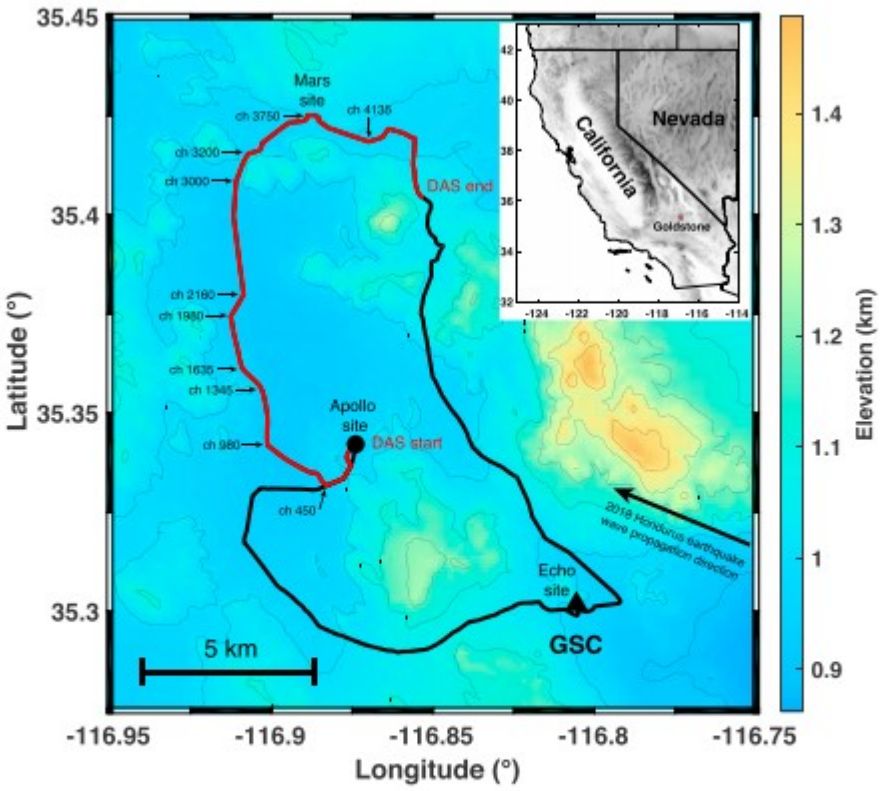


**Figure 1.** Map showing the location of telecommunication fiber optic cables around the Goldstone Deep Space Communications Complex. The Goldstone OpticaL Fiber Seismic experiment acquires DAS data along a ~20-km segment (red line) of the total ~50-km-long cable (dark line). Some key channel numbers are labeled. Solid triangle marks the broadband seismometer GSC. The thick arrow shows the horizontal wave propagation direction of the seismic waves from the 2018 Honduras earthquake. DAS = distributed acoustic sensing.

## 2.3 The 2018 Honduras M7.5 Earthquake

During the 3-month deployment of the GOLFS experiment, three teleseismic events with $M_w \geq 6.5$ are recorded (Table S1). The largest magnitude event is the 2018 M7.5 Honduras earthquake (17.483°N, 83.520°W; 19-km depth; 10 January 2018, 02:51:33.3 UTC; earthquake catalog from U.S. Geological Survey [USGS] National Earthquake Information Center). DAS clearly records the waveform of this event (Figure 2a). Major body waves (*P*, *PP*, and *S*) and surface waves (Rayleigh and Love waves) can be identified. For the other two events with smaller magnitude and larger epicentral distance, surface waves are clearly observed, but body waves are close to the noise level (supporting information Figure 2). We will focus our study on the Honduras earthquake only. We also stack DAS strains over hundreds of meters (still much less than teleseismic wavelengths) in order to enhance the signal-to-noise ratio, although the following analyses are essentially the same for single DAS channels.

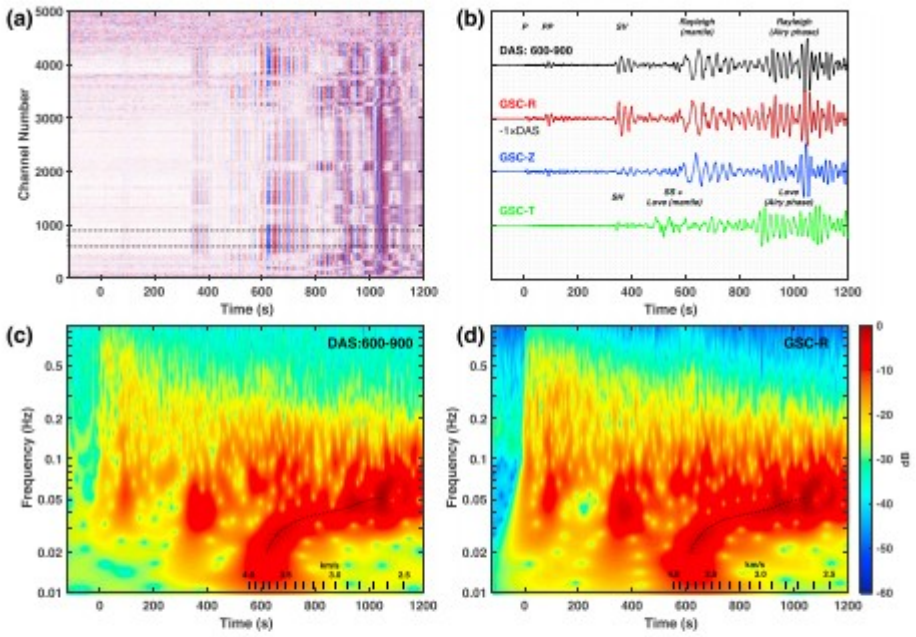


**Figure 2.** Data from the 2018 M7.5 Honduras earthquake recorded on DAS channels and GSC broadband seismometer. (a) Waveform data of all ~5,000 DAS channels from the Goldstone OpticaL Fiber Seismic experiment. The channel spacing is 4 m. (b) Comparison between selected DAS strain and GSC particle velocity. The GSC waveforms are rotated into vertical, radial, and tangential components after removing the instrument response. Waveforms are band-pass filtered between 0.01 and 2 Hz. Amplitudes are normalized to unity by the peak amplitude of DAS strain and radial GSC velocity, respectively. The selected DAS strain is stacked from channels 600–900. For better comparison, polarity-reversed DAS strain (dash line) is also plotted, overlying the radial GSC velocity. (c, d) The spectrograms of the stacked DAS strain and radial-component GSC velocity, respectively. The dash line tracks the Rayleigh wave group velocity dispersion. The group velocity scale is shown at the bottom. DAS = distributed acoustic sensing.

The reliability of DAS recordings is demonstrated through their comparison with particle velocity of the broadband GSC station. For example, stacked DAS strain waveform from channels 600 to 900, whose orientations are close to the wave propagation direction, shows excellent consistency with the radial component GSC velocity waveform (Figure 2b). There is a polarity flip between these two measurements, consistent with their intrinsic relationship in equation 1. A time delay of ~2.8 s due to difference in epicentral distance is corrected (Figure 1). Both traces are normalized by the maximum amplitude of the Rayleigh wave (airy phase at a period ~20 s). As a result of higher apparent phase velocity, major body wave phases (*P*, *PP*, and *SV*) show relatively larger amplitudes on GSC velocity waveform than on DAS strain waveform (Figure 2b; equation 1). Time-frequency analysis (Stockwell et al., 1996) suggests similar spectrum pattern between stacked DAS strain and GSC particle velocity, but the relative noise level of the former is about 20–30 dB higher than that of the latter (cf. Figures 2c and 2d). The recorded DAS waveforms show strong orientation dependency as expected for horizontal strain measurements (Figure 2a; supporting information).

## 3 Results

### 3.1 DAS Receiver Functions

For teleseismic *P* and *SV* incidence, DAS strains are expected to be in phase for all azimuths and to be the same as radial-component particle velocity (except for a polarity reversal and amplitude scaling). To this end, conventional receiver function analysis can be extended to DAS strain measurements with additional knowledge of the incident source wavelet. Here we use the vertical-component particle velocity at GSC as an approximation of the incident source wavelet to deconvolve the DAS strains. We use both time-domain iterative deconvolution (Ligorria & Ammon, 1999) and frequency-domain water level deconvolution (Langston, 1979) algorithms to compute receiver functions. Time delays of the stacked DAS channels are corrected by cross correlating them with the polarity-reversed radial-component GSC velocity. Amplitudes are normalized after source deconvolution.

Figure 3a shows stacked DAS strains for several selected channels. Albeit with higher noise level, all of them show consistent, in-phase waveforms that are polarity-reversed from the GSC radial-component velocity. For this event, Moho *Ps* conversion and its multiple *PpPs* can be clearly identified on the GSC receiver function using both source deconvolution algorithms. DAS receiver functions also show clear Moho *Ps* conversion on all selected channels, but the crustal multiple *PpPs* does not show up coherently (Figures 3b and 3c). Looking more closely, there are subtle but observable differences in the arrival times of Moho conversions between DAS and GSC receiver functions. Most DAS channels have delayed *Ps* arrivals compared with that on GSC (Figures 3b and 3c). The *PpPs* phase also seems delayed on channels 600-700, 700-800, and 800-900 (Figure 3c). These changes are likely caused by lateral variations in crustal structure. For example, assuming a nominal crustal Poisson's ratio of 0.25, the *Ps* arrival times suggest an increase of crustal thickness by about 2 km, from ~26 km beneath GSC to ~28 km beneath channels 600-700, consistent with those of Yan and Clayton (2007). Therefore, with dense DAS arrays, it is possible to track fine-scale lateral variations in crustal structure, especially if the noise level of DAS waveforms can be further reduced.

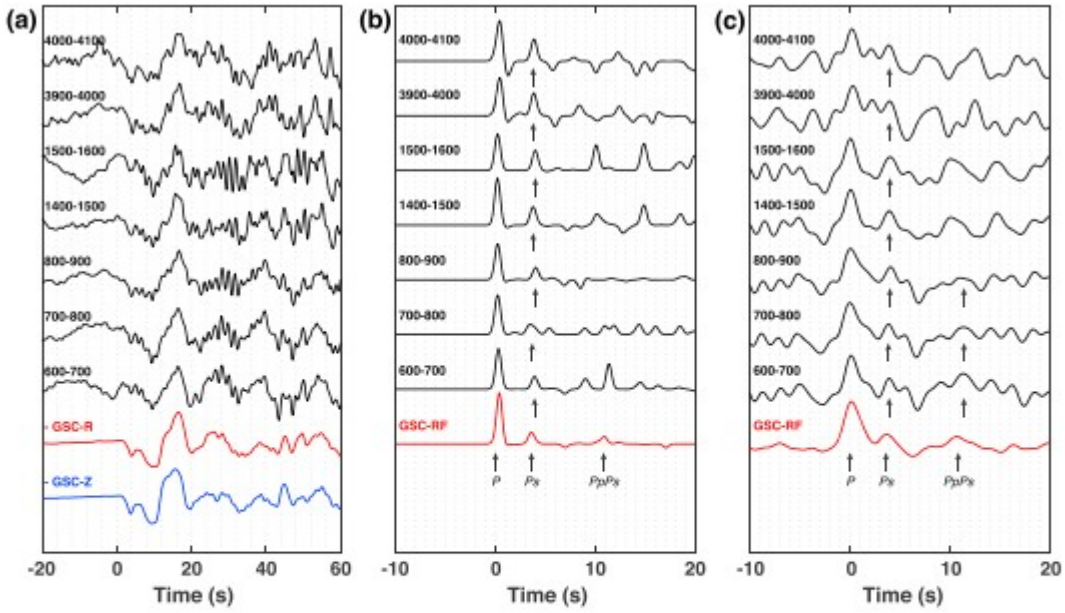


**Figure 3.** *P* wave receiver functions for selected DAS channels and GSC station. (a) Stacked DAS strains and GSC radial- and vertical-component velocities in the *P* wave train. For better comparison, GSC velocities are polarity reversed. (b) Receiver functions for DAS and GSC calculated with time-domain iterative deconvolution. A band-pass filter between 0.02 and 1 Hz is applied. (c) Same as (b) but using the frequency-domain water level deconvolution algorithm. The water level is fixed at 0.01 of the maximum spectrum amplitude. Note, all DAS receiver functions show clear Moho Ps conversion, albeit with higher noise level compared with that of GSC. DAS = distributed acoustic sensing.

## 3.2 Arrival Time Picking

We derive densely distributed arrival time measurements by cross-correlating DAS strain on each channel with the horizontally rotated velocity records measured at GSC. We systematically search all azimuths to find the optimal orientation that gives highest cross-correlation coefficient between observed DAS strain and rotated GSC velocity (Figure 4a). In this way, we can simultaneously estimate the time delay and orientation of each DAS channel. The underlying assumption of such practice is that the wave train should contain both in-plane (*P-SV* or Rayleigh wave) and out-of-plane (*SH* or Love wave) particle motions. If the wave train contains in-plane or out-of-plane particle motions only, additional information on absolute amplitudes are required to estimate DAS orientations.

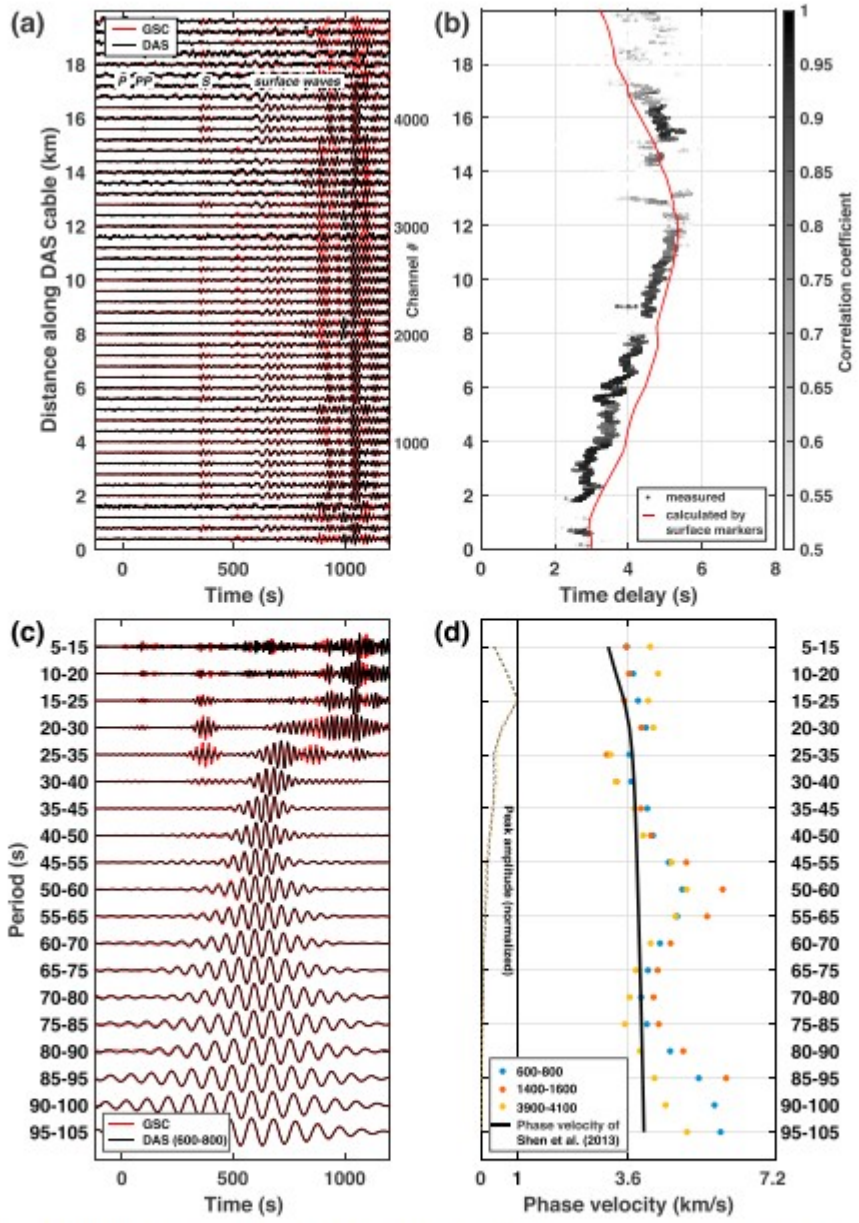


**Figure 4.** Arrival time and local Rayleigh wave dispersion estimation for DAS channels. (a) DAS strains at every 100 channels and their best fit GSC horizontal velocities. (b) Estimated arrival time delays of all DAS channels with respect to the nearby GSC station. Channels with low cross-correlation coefficient (<0.5) are not shown. The red line shows the calculated time delays of the DAS cable using its surface markers indicating the DAS cable route. A constant phase velocity of 2.5 km/s is used. (c) Comparison of narrowband-passed waveforms between DAS strain (channels 600–800) and radial-component GSC velocity. Amplitudes are normalized to unity at each frequency bands. (d) Estimated local Rayleigh wave dispersion from 10 to 100 s. The black line is the expected Rayleigh wave dispersion curve from Shen et al. (2013). Thin dashed lines are the peak amplitudes at different periods (normalized by their maximum values at 20 s). DAS = distributed acoustic sensing.

Figure 4b shows estimated arrival time delays of all DAS channels with respect to the GSC station. Since we use the entire wave train, −120 s before and 1,200 s after the *P* wave arrival, the measured arrival time delays mainly reflect those of high-amplitude surface waves (Figure 2). Using narrow time windows to exclude major body waves have little effect on the results. The estimated arrival time delays as well as DAS orientations are generally consistent with those calculated by surface markers indicating the DAS cable

route (Figures 4b and supporting information Figure S3). However, one-to-one comparison is difficult, as the buried DAS cable geometry is likely to be different from the linear interpolation of surface markers. In fact, there seems to be a constant shift along the distance axis between them (Figure 4b), which could be due to excess fiber near the starting point. Attempts are also made to estimate individual body wave arrival time delays, but they are more scattered due to lower signal-to-noise ratio (supporting information Figure S4).

## 3.3 Surface Wave Analysis

### *3.3.1 Path-Averaged Group Velocity Measurement*

Spectrograms in Figures 2c and 2d clearly show the dispersion of Rayleigh wave group velocity, which is similar for DAS stains and the GSC particle velocity. We measure the Rayleigh wave group arrivals at each period between 20 and 50 s by tracking their maximum peaks in the time-frequency domain (Figure 2c and 2d). Then, we calculate path-averaged Rayleigh wave group velocity by taking the ratio of epicentral distance and Rayleigh wave group travel times. Results (e.g., dashed lines in Figures 2c and 2d) show that the average Rayleigh wave group velocity increases from 2.64 km/s at 20 s to 3.76 km/s at 50 s. Group velocity in this frequency range is mostly sensitive to the shear wave velocity structure in the lower crust and uppermost mantle along the path. Similar measurements can potentially be made for regional earthquakes and ambient noise correlations in the future to shorter periods, especially if region-scale DAS arrays become available.

### *3.3.2 Local Phase Velocity Measurement*

We measure Rayleigh wave amplitude ratios between particle velocities on GSC and strains on DAS channels for various narrow-passed frequency bands. To minimize phase interference, we only select DAS channels whose orientations are close to the wave propagation direction. The horizontal GSC velocity is rotated to its radial component. Figure 4c shows the comparison of narrowband waveforms between GSC radial velocity and stacked DAS strain from channels 600–800. They are generally in good consistency even up to periods of 100 s. As absolute values of dynamic strain on DAS channels are somewhat uncertain, we normalize all measured Rayleigh wave amplitude ratios by the amplitude ratio of nondispersive *SV* at a central period of 30 s, where the *SV* wave is most clear. The phase velocity of *SV* wave is 7.2 km/s, calculated using the TauP toolkit (Crotwell et al., 1999) and the *ak135* reference model (Kennett et al., 1995).

Figure 4d shows the estimated Rayleigh wave phase velocity dispersion for several selected DAS segments. The estimated dispersion curves are generally consistent among each other. At short periods (<50 s), estimated Rayleigh wave phase velocities are located near the expected dispersion curve from previous studies (Shen et al., 2013), with deviations on the order of 10–20%. However, a sudden decrease at ~30 s and large perturbations at

>50 s are not consistent with the expected smooth, monotonic increase in Rayleigh wave phase velocity with period.

## 4 Discussions

### 4.1 Possible Causes of Deviations in Local Surface Wave Phase Velocity Measurement

Our study shows relatively large uncertainties in local surface wave phase velocity measurement, especially at a period of ~60 s (Figure 4d). The large uncertainty is unlikely to be caused by one-dimensional crust and mantle velocity structures, as any realistic models will produce smooth, monotonic increase in Rayleigh wave phase velocity at long periods.

Previous studies also reported inaccuracy in phase velocity estimation using the amplitude ratios of colocated velocity and strain seismometers (Gomberg & Agnew, 1996; Mikumo & Aki, 1964). Mikumo and Aki (1964) found good agreement between calculated and theoretically predicted phase velocities for body waves but not for surface waves. Gomberg and Agnew (1996) compared dynamic strains estimated from broadband seismometers with strains recorded by a three-component long-base strainmeter at Pinon Flat observatory. They found that although the phase of the estimated strain matches that of the observed strain quite well, the amplitudes are often systematically off.

A few possibilities might cause the deviation in estimated Rayleigh wave phase velocity. First, the peak amplitudes of surface waves decrease significantly beyond about 20 s (Figure 4d), which may result in large uncertainties in the calculated amplitude ratios at long periods. Second, DAS channels are not colocated with the GSC broadband seismometer (Figure 1). We expect that difference in distance alone has a minor effect on the result, as the amplitude of teleseismic body and surface waves should vary smoothly over distance (except near caustics). However, effects of lateral structural heterogeneity may invalidate the plane wave assumption for equation 1. In addition, site effects are likely different between DAS channels and the GSC station (Figure 1). As such, the Rayleigh wave amplitude may have a strong lateral variation. Gomberg and Agnew (1996) attributed the inconsistency of dynamic strains estimated from colocated strainmeter and seismometer to lateral material heterogeneities and topography. Third, in our analysis, we assume a flat frequency response of DAS strain measurements. Jousset et al. (2018) used the strain response of an impulse displacement signal to calibrate the instrument response of DAS records. They found a linear increase in amplitude response with frequency below 100 Hz (in logarithm versus logarithm scale). Such instrument response characteristics can cause systematic bias in estimated Rayleigh wave phase velocity, but it is difficult to explain the large perturbation in Figure 4d. Finally, the DAS cable coupling may also vary along the array. If the cable contacts the side of the conduit loosely or sections include double conduit designs, the amplitude response may be quite different and likely be

frequency dependent (Kuvshinov, 2016). Future studies are needed to better quantify the frequency response and coupling of DAS considering the heterogeneous installation conditions encountered when utilizing telecom infrastructure.

### 4.2 Limitations and Opportunities for DAS in Passive Seismology

We have demonstrated three potential applications of DAS in teleseismic studies. The dense distribution of strain or strain rate sensors is one of the major advantages of DAS over conventional seismometers. Densely spaced arrival time measurement and receiver function analysis can be used to study fine-scale structure of the crust and upper mantle. The broadband nature of DAS strain measurements can potentially be used for surface-wave or normal-mode analysis in the future. Another great advantage of DAS is that it only requires an interrogation unit at one end of a telecommunication fiber optic cable, which makes it cost effective and easy to implement. There is already a vast installed base of telecommunication cables around the world; opportunistic DAS deployments utilizing this resource provide a low-cost approach for dense array acquisition. In some harsh environment, such as offshore, where conventional seismic deployment is difficult, DAS may be of more value in terms of seismic monitoring, subsurface imaging, and hazard assessment.

One of the current limitations of DAS is its higher noise level than conventional broadband seismometers. For the 2018 Honduras earthquake, it is clear that the signal-to-noise ratio of DAS is much lower than that of the nearby GSC station (cf. Figures 2c and 2d). This is especially true for teleseismic body waves, since they travel steeply near the surface and have a high apparent phase velocity. In an extreme case, sensitivity to vertically incident body waves should be 0 for horizontally oriented DAS. As a result, teleseismic body waves are barely observed on horizontal DAS channels for smaller magnitude earthquakes (supporting information Figure S2). Nevertheless, with further development on the DAS technology and possibly optimal design of recording geometry, DAS is likely to play an important role in passive seismology studies, such as high-resolution seismic tomography and structural imaging.

## 5 Conclusions

In 2017 and 2018, a new DAS field experiment was carried out in Goldstone, California. Using waveform data from the 10 January 2018 M7.5 Honduras earthquake, we explore three potential applications of DAS in teleseismic studies. First, DAS receiver functions are calculated by deconvolving vertical-component GSC velocity from DAS strains. Moho signals are clearly visible on DAS receiver functions. Second, dynamic strains on DAS can provide densely distributed travel time measurements. Third, path-averaged Rayleigh wave group velocity and local Rayleigh wave phase velocity are estimated. The latter is based on intercomparison of waveforms from the GSC velocity seismometer and DAS strainmeters, but the result is less certain. In the near

future, with further technical development, DAS will likely play an important role in many fields of passive seismology.

## Acknowledgments

We thank Greg Anderson, Mark Chen, Michael Lucero, Rosemary Cobb, Gary Warnick, and Jose Perez from the JPL Deep Space Network (DSN) for permission to use the optical fiber and assistance in data collection. We would also like to thank Silixa for DAS acquisition support during the GOLFS deployment. Constructive comments from editor Jeroen Ritsema, Nori Nakata and an anonymous reviewer are appreciated. This work is partially supported by the National Science Foundation Grants 1722879 and 1829496, the Caltech Discovery Fund, and the President's and Director's Fund. J. Ajo-Franklin, M. Robertson, and DAS acquisition efforts were supported by the Laboratory Directed Research and Development (LDRD) Program of Lawrence Berkeley National Laboratory under U.S. Department of Energy Contract DE-AC02-05CH11231. Field support was provided by the Geoscience Measurement Facility (GMF), Earth and Environmental Sciences Area, and Lawrence Berkeley National Laboratory. N. Lindsey was supported by the National Science Foundation Graduate Research Fellowship under Grant DGE 1106400. Broadband seismic waveform data for the GSC station are retrieved from the Caltech/USGS SCSN (doi:10.7914/SN/CI) stored at SCEDC (doi:10.7909/C3WD3xH1).

## References

Agnew, D. C. (1986). Strainmeters and tiltmeters. *Reviews of Geophysics*, 24( 3), 579– 624. https://doi.org/10.1029/RG024i003p00579

Ajo-Franklin, J. B., Dou, S., Lindsey, N. J., Monga, I., Tracy, C., Robertson, M., Tribaldos, V. R., Ulrich, C., Freifeld, B., Daley, T., & Li, X. (2019). Distributed acoustic sensing using dark fiber for near-surface characterization and broadband seismic event detection. *Scientific Reports*, 9, 1328. https://doi.org/10.1038/s41598-018-36675-8

Bakku, S. K. (2015). Fracture characterization from seismic measurements in a borehole. *PhD Thesis,* Massachusetts Institute of Technology.

Becker, M. W., Ciervo, C., Cole, M., Coleman, T., & Mondanos, M. (2017). Fracture Hydromechanical response measured by fiber optic distributed acoustic sensing at milliHertz frequencies: Fracture hydromechanics from DAS. *Geophysical Research Letters*, 44, 7295– 7302. https://doi.org/10.1002/2017GL073931

Benioff, H. (1935). A linear strain seismograph. *Bulletin of the Seismological Society of America*, 25( 4), 283– 309.

Crotwell, H. P., Owens, T. J., & Ritsema, J. (1999). The TauP toolkit: Flexible seismic travel-time and ray-path utilities. *Seismological Research Letters*, 70( 2), 154– 160. https://doi.org/10.1785/gssrl.70.2.154

Daley, T. M., Miller, D. E., Dodds, K., Cook, P., & Freifeld, B. M. (2016). Field testing of modular borehole monitoring with simultaneous distributed acoustic sensing and geophone vertical seismic profiles at Citronelle, Alabama. *Geophysical Prospecting*, 64( 5), 1318– 1334. https://doi.org/10.1111/1365-2478.12324

Daley, T. M., Freifeld, B. M., Ajo-Franklin, J., Dou, S., Pevzner, R., Shulakova, V., Kashikar, S., Miller, D. E., Goetz, J., Henninges, J., & Lueth, S. (2013). Field testing of fiber-optic distributed acoustic sensing (DAS) for subsurface seismic monitoring. *The Leading Edge*, 32( 6), 699– 706. https://doi.org/10.1190/tle32060699.1

Dou, S., Lindsey, N., Wagner, A. M., Daley, T. M., Freifeld, B., Robertson, M., Peterson, J., Ulrich, C., Martin, E. R., & Ajo-Franklin, J. B. (2017). Distributed acoustic sensing for seismic monitoring of the near surface: A traffic-noise interferometry case study. *Scientific Reports*, 7( 1), 11620. https://doi.org/10.1038/s41598-017-11986-4

Gomberg, J., & Agnew, D. (1996). The accuracy of seismic estimates of dynamic strains: An evaluation using strainmeter and seismometer data from Piñon Flat Observatory, California. *Bulletin of the Seismological Society of America*, 86( 1A), 212– 220.

Grattan, L. S., & Meggitt, B. T. (2000). *Optical fiber sensor technology: Fundamentals*. Boston: Springer.

Hartog, A., Frignet, B., Mackie, D., & Clark, M. (2014). Vertical seismic optical profiling on wireline logging cable. *Geophysical Prospecting*, 62( 4), 693– 701. https://doi.org/10.1111/1365-2478.12141

Jousset, P., Reinsch, T., Ryberg, T., Blanck, H., Clarke, A., Aghayev, R., Hersir, G. P., Henninges, J., Weber, M., & Krawczyk, C. M. (2018). Dynamic strain determination using fibre-optic cables allows imaging of seismological and structural features. *Nature Communications*, 9( 1), 2509. https://doi.org/10.1038/s41467-018-04860-y

Kennett, B., Engdahl, E., & Buland, R. (1995). Constraints on seismic velocities in the Earth from traveltimes. *Geophysical Journal International*, 122( 1), 108– 124. https://doi.org/10.1111/j.1365-246X.1995.tb03540.x

Kuvshinov, B. (2016). Interaction of helically wound fibre-optic cables with plane seismic waves. *Geophysical Prospecting*, 64( 3), 671– 688. https://doi.org/10.1111/1365-2478.12303

Langston, C. A. (1979). Structure under Mount Rainier, Washington, inferred from teleseismic body waves. *Journal of Geophysical Research*, 84( B9), 4749– 4762. https://doi.org/10.1029/JB084iB09p04749

Langston, C. A., & Liang, C. (2008). Gradiometry for polarized seismic waves. *Journal of Geophysical Research*, 113, B08305. https://doi.org/10.1029/2007JB005486

Li, Z., & Zhan, Z. (2018). Pushing the limit of earthquake detection with distributed acoustic sensing and template matching: A case study at the Brady geothermal field. *Geophysical Journal International*, 215( 3), 1583– 1593. https://doi.org/10.1093/gji/ggy359

Ligorria, J. P., & Ammon, C. J. (1999). Iterative deconvolution and receiver-function estimation. *Bulletin of the Seismological Society of America*, 89( 5), 1395– 1400.

Lindsey, N. J., Martin Eileen, R., Dreger Douglas, S., Barry, F., Stephen, C., James Stephanie, R., et al. (2017). Fiber-optic network observations of earthquake wavefields. *Geophysical Research Letters*, 44, 11,792– 11,799. https://doi.org/10.1002/2017GL075722

Lumens, P. G. E. (2014). Fibre-optic sensing for application in oil and gas wells. *PhD Thesis, Eindhoven University of* Technology

Martin, E. R., Lindsey, N., Ajo-Franklin, J., & Biondi, B. (2018). Introduction to interferometry of fiber optic strain measurements. *EarthArXiv*.

Mateeva, A., Lopez, J., Potters, H., Mestayer, J., Cox, B., Kiyashchenko, D., Wills, P., Grandi, S., Hornman, K., Kuvshinov, B., Berlang, W., Yang, Z., & Detomo, R. (2014). Distributed acoustic sensing for reservoir monitoring with vertical seismic profiling. *Geophysical Prospecting*, 62( 4), 679– 692. https://doi.org/10.1111/1365-2478.12116

Mateeva, M., Cox, B., Kiyashchenko, D., Wills, P., Lopez, J., et al. (2012). Advances in distributed acoustic sensing (DAS) for VSP. In *SEG Technical Program Expanded Abstracts 2012* (pp. 1– 5). Tulsa: Society of Exploration Geophysicists.

Mikumo, T., & Aki, K. (1964). Determination of local phase velocity by intercomparison of seismograms from strain and pendulum instruments. *Journal of Geophysical Research*, 69( 4), 721– 731. https://doi.org/10.1029/JZ069i004p00721

Miller, D., Parker, T., Kashikar, S., Todorov, M., & Bostick, T. (2012). Vertical seismic profiling using a fibre-optic cable as a distributed acoustic sensor. Presented at the 74th EAGE Conference and Exhibition incorporating EUROPEC 2012.

Posey, J. R., Johnson, G., & Vohra, S. (2000). Strain sensing based on coherent Rayleigh scattering in an optical fibre. *Electronics Letters*, 36( 20), 1.

Shen, W., Ritzwoller, M. H., & Schulte-Pelkum, V. (2013). A 3-D model of the crust and uppermost mantle beneath the Central and Western US by joint inversion of receiver functions and surface wave dispersion. *Journal of Geophysical Research: Solid Earth*, 118, 262– 276. https://doi.org/10.1029/2012JB009602

Stockwell, R. G., Mansinha, L., & Lowe, R. (1996). Localization of the complex spectrum: The S transform. *IEEE Transactions on Signal Processing*, 44( 4), 998– 1001. https://doi.org/10.1109/78.492555

Wang, H. F., Zeng, X., Miller, D. E., Fratta, D., Feigl, K. L., Thurber, C. H., & Mellors, R. J. (2018). Ground motion response to an ML 4.3 earthquake using co-located distributed acoustic sensing and seismometer arrays. *Geophysical Journal International*, 213( 3), 2020– 2036. https://doi.org/10.1093/gji/ggy102

Yan, Z., & Clayton, R. W. (2007). Regional mapping of the crustal structure in southern California from receiver functions. *Journal of Geophysical Research*, 112, B05311. https://doi.org/10.1029/2006JB004622

Zeng, X., Lancelle, C., Thurber, C., Fratta, D., Wang, H., Lord, N., Chalari, A., & Clarke, A. (2017). Properties of noise cross-correlation functions obtained from a distributed acoustic sensing array at Garner Valley, California. *Bulletin of the Seismological Society of America*, 107( 2), 603– 610. https://doi.org/10.1785/0120160168